RESEARCH ARTICLE

A new approach to characterize firebrand showers using advanced 3D imaging techniques

Nicolas Bouvet[1] · Eric D. Link[1] · Stephen A. Fink[1]

Abstract

A new approach to characterize airborne firebrands during Wildland-Urban Interface (WUI) fires is detailed. The approach merges the following two imaging techniques in a single field-deployable diagnostic tool: (1) 3D Particle Tracking Velocimetry (3D-PTV), for time-resolved mapping of firebrand 3D trajectories, and (2) 3D Particle Shape Reconstruction (3D-PSR), to reconstruct 3D models of individual particles following the Visual Hull principle. This tool offers for the first time the possibility to simultaneously study time-resolved firebrand fluxes and firebrand size distribution to the full extent of their three-dimensional nature within a control volume. Methodologies used in the present work are presented and their technical implementation is discussed. Validation tests to confirm proper tracking/sizing of particles are detailed. The diagnostic tool is applied to a firebrand shower artificially generated at the NIST National Fire Research Laboratory. A novel graphic representation, that incorporates both the Cumulative Particle Count (CPC, particles m^{-2}) and Particle Number Flux (PNF, particles m^{-2} s^{-1}) as relevant exposure metrics, is presented and the exposure level is compared to that of an actual outdoor fire. Size distributions obtained for airborne firebrands are compared to those achieved through ground collection and strategies to improve the particle shape reconstruction method are discussed.

Graphic abstract
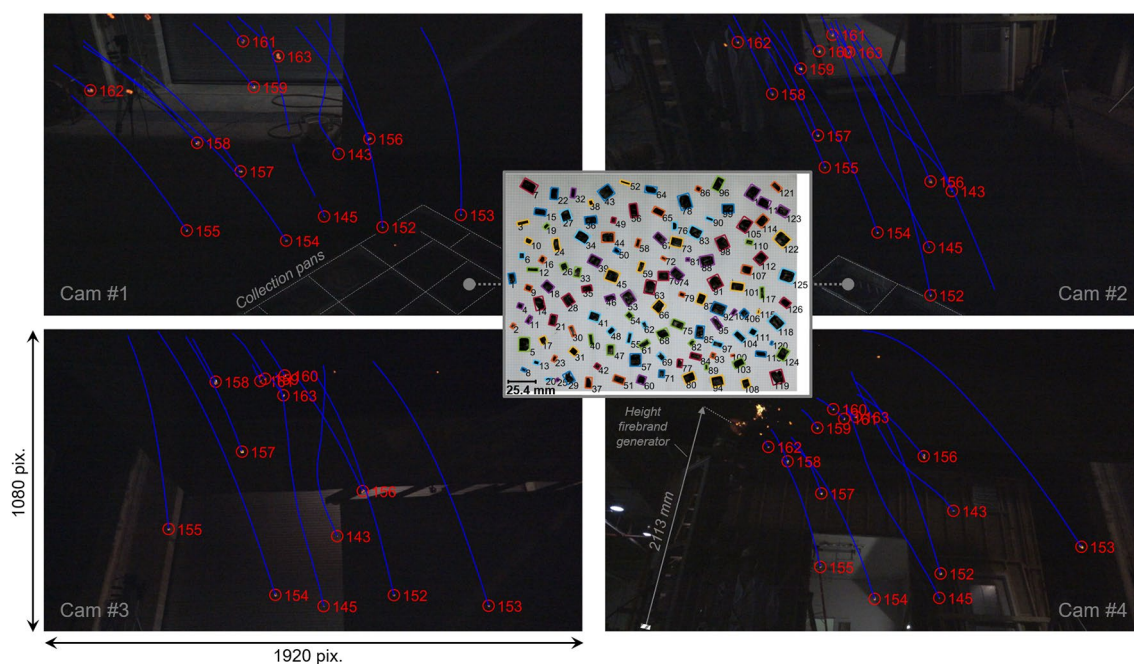
1 Introduction

It has been recently established that fire weather season length has increased globally by almost 19% between 1979 and 2013 (Jolly et al. 2015). Continuation of such a trend, coupled with fuel and ignition sources availability, would lead to a global wildfire potential increase with significant socio-economic and ecological impacts (Jolly et al. 2015). In the USA, this analysis is backed-up by staggering statistics: out of the top ten most destructive California wildfires, seven occurred in the past five years, totaling over 420,000 burned hectares, over 32,000 destroyed structures and over 120 fatalities (Calfire 2020).

A challenging aspect of wildland and Wildland-Urban Interface (WUI) fires is that large amounts of firebrands (often referred to as "embers") are usually produced from the burning of vegetative and structural fuels. These firebrands often become airborne and can be transported over long distances away from their origin. If they carry enough energy, they may ignite recipient fuels and, in turn, initiate new fire fronts, rendering suppression activities extremely difficult. It is not uncommon to witness "rains" or "showers" of firebrands impacting WUI areas, a recent example being the Coffey Park neighborhood in Santa Rosa, CA, during the Tubbs Fire in 2017 (Bermudez et al. 2017). This problem is of great importance since firebrands may cause up to 90% of home and business ignitions during wildfire events (Insurance Institute for Business & Home Safety 2019).

There have been quite a few efforts to characterize firebrands generated by structural or vegetative fuels, in both lab-scale [e.g., Waterman (1969), Manzello et al. (2009)] and outdoor [e.g., Vodvarka (1970), Thomas et al. (2017)] fire configurations. However, strong limitations remain given the nature of the chosen approaches. For instance, bulk flow characteristics (e.g.,particle number flux, mass flux) are intrinsically time-averaged, hence information regarding instantaneous intensity of the firebrand showers is often unavailable. Studies that have shown some temporal resolution ability using 2D imaging devices [see Filkov et al. (2017), Filkov and Prohanov (2018) and Tohidi et al. (2017)] are somewhat hindered by the lack of volumetric resolution, which renders measurements of instantaneous particle fluxes extremely challenging. In addition, bulk flow characteristic studies seem to exclusively focus on vertical transport of firebrands (with respect to the gravity direction), while horizontal transport is usually overlooked, although likely important in many practical situations (e.g., exposure severity assessment in the vicinity of structures with exposed vents, rate of firebrand deposition vs downstream transport ahead of a fire line, etc.). With a few exceptions (El Houssami et al. 2016; Manzello et al. 2007, 2009), individual particle characteristics (e.g., firebrand size/shape) suffer from a purely 2D treatment, a firebrand projected area being considered as the sole metric. Firebrand dimensions, volumes and shapes have been mostly undetermined or neglected, although such attributes are likely to govern the formation of aggregates and trapping in complex geometries (screen mesh, crevices, etc.).

The limitations highlighted above clearly stress the need for new ways to characterize firebrand showers in the context of their three-dimensional nature, both at the macroscopic and microscopic levels. Therefore, the present work is devoted to the development and validation of a diagnostic tool designed to overcome these limitations by allowing full spatio-temporal resolution of airborne firebrand flows. To do so, this new tool merges two optical techniques, 3D Particle Tracking Velocimetry (3D-PTV) (Maas 1991; Maas et al. 1993) and 3D Particle Shape Reconstruction (3D-PSR) [via the Visual Hull concept, see Laurentini (1994)] in a single field-deployable device, referred to as "emberometer". Both techniques, rather well-established, rely on close-range photogrammetry principles and the reader is referred to reference textbooks, e.g., Luhmann et al. (2014), for a detailed account of core principles.

The paper is organized as follows: Section 2 provides a brief overview of the 3D-PTV/PSR system that was developed and includes the hardware presentation and details about the methodology implementation. Examples of experimental validations performed for both particle tracking and sizing steps are given in Sect. 3. The system is applied to an artificially generated firebrand shower in Sect. 4. Particle tracking and sizing results are discussed and a new visualization tool for firebrand flux analysis is proposed. Final remarks are provided in Sect. 5, followed by the conclusion in Sect. 6.

Unless mentioned otherwise, all uncertainties are reported as expanded uncertainties, $X \pm ku_c$, from a combined standard uncertainty (estimated standard deviation) u_c, and a coverage factor $k = 2$ (95% confidence level, assuming normal distribution of the data). Additional details are provided in Bouvet et al. (2020).
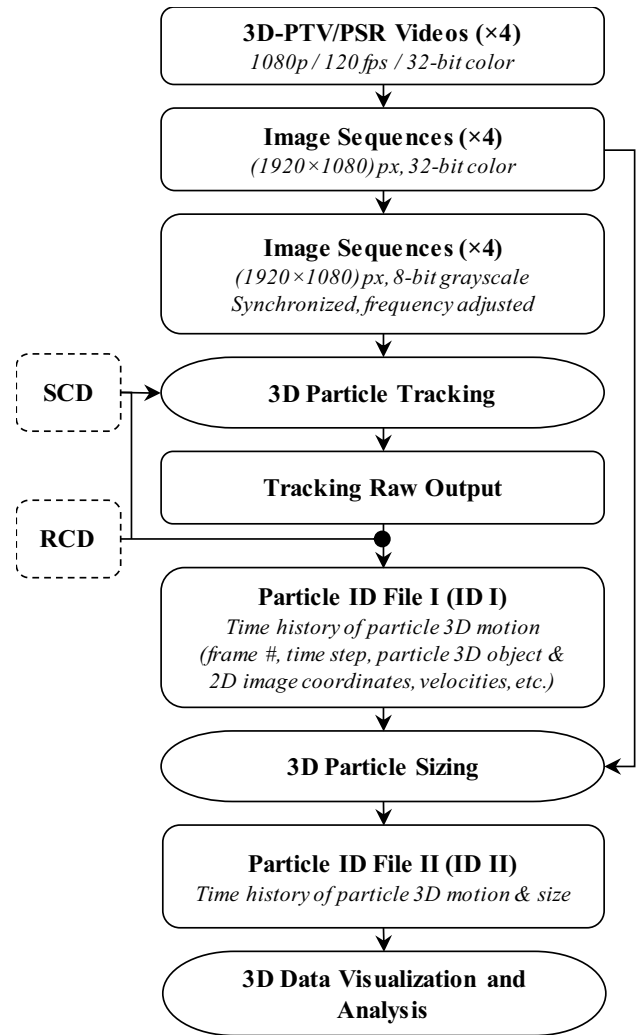
2 3D-PTV/PSR system

2.1 System overview[1]

The 3D representation of the 3D-PTV/PSR system is shown in Fig. 1. The system is composed of four compact cameras (*Sony DSC-RX10 M3*, ≈ 20 Megapixels) with large

---

[1] Certain commercial equipment, instruments, or materials are identified in this paper in order to specify the experimental procedure adequately. Such identification is not intended to imply recommendation or endorsement by the National Institute of Standards and Technology, nor is it intended to imply that the materials or equipment identified are necessarily the best available for the purpose.
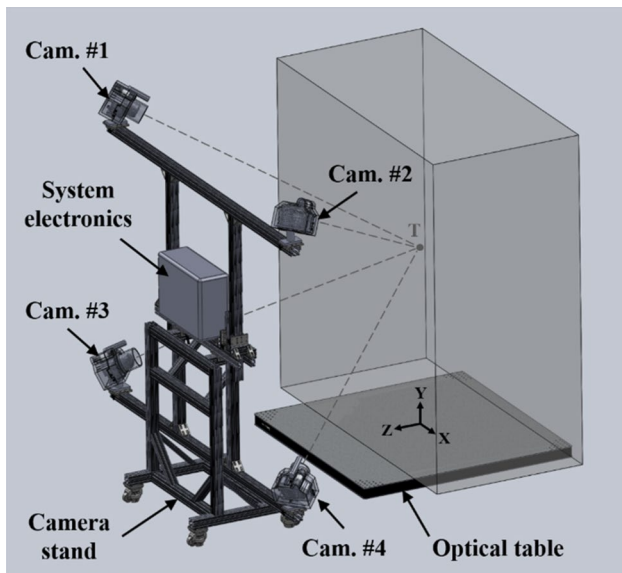
Fig. 1 3D-PTV/PSR system experimental layout: 3D representation of the apparatus (the volume above the optical table shows the actual footprint of the spatial calibration target shown in Fig. 3, the table top is raised by about 0.235 m from the ground)

Fig. 2 System processing flowchart (SCD: Spatial Calibration Data, RCD: Resolution Calibration Data)

diameter built-in lenses. The cameras are located at both ends of two horizontal rails (length: 2.03 m), whose upper faces are adjusted at a 0.356 m and 1.880 m height, respectively. For calibration/validation, the stand is anchored to an optical table (≈ 1.22 m $\times 1.22$ m) located 0.559 m away from the camera plane, which provides a convenient fixed reference origin in the object space. Camera orientations are manually adjusted using tripod heads so that image centers closely coincide with a known target point T in the object space [coordinates (0 m, 1.041 m, 0 m)], on which focus is performed. Cameras are operated at minimum focal length ($f = 8.8$ mm) and largest aperture ($f/2.4$). The system control volume, defined as the intersection of the camera field of views, is estimated to be ≈ 1.91 m^3. Video stream synchronization was performed post-acquisition based on the disappearance of a small laser dot visible from all cameras. The system processing flowchart is provided in Fig. 2. Videos acquired by the 3D-PTV/PSR system are rendered into image sequences by extracting individual video frames via a commercial software. Image sequences are then synchronized and transposed into grayscale color space using an in-house MATLAB code. If necessary, the code allows for sequence downsampling to reduce computational burden for the 3D tracking step. Grayscale image sequences are then processed by the PTV software, in conjunction with the spatial calibration data (SCD—see additional details in Sect. 2.2). An in-house FORTRAN code generates individual particle "identity" files (ID I) that gather time-stamped particle motion characteristics from the tracking step raw

outputs. A dedicated calibration procedure is used to generate local Resolution Calibration Data (RCD—i.e., an effective local resolution in mm/pixel given a particle 3D location) used for particle sizing purposes. The color image sequences and selected data from ID I files (particle image 2D coordinates, particle 3D coordinates and associated local resolutions) are then used for particle sizing purposes (see details in Sect. 2.3). Particle tracking and sizing results are compiled in particle ID files II (ID II) that are used for 3D data visualization and analysis.

Given the current technical implementations, the system is expected to consistently detect and process glowing particles with characteristic dimensions ranging from 2 mm to multi-centimeter lengths (validation tests, not reported here, showed that 51 mm wide disks could be successfully tracked and reconstructed). The 2-mm size limit is a conservative estimate based on the lowest spatial resolution achieved

within the control volume and a minimum particle image size of 1 pixel. Resolved firebrand velocities ranging from 0.27 m s^{-1} to at least 18 m s^{-1} are to be expected for flow conditions similar to those discussed in Sect. 4 and a data acquisition frequency of 120 fps. Note here that the lower velocity limit is obtained assuming a 1-pixel particle image diameter (i.e., no subpixel accuracy in particle image location), a 1-pixel diagonal displacement, a spatial resolution of 1.6 mm/pix and a particle image visible in two consecutive frames only. For particle images visible in multiple recordings along the time-resolved sequence, this limit may be lower since intermediate frames could be skipped (with the limit of making use of the first and last recorded frames only).

2.2 Firebrand tracking using 3D particle tracking velocimetry (3D-PTV)

The 3D tracking of firebrands is computed via the opensource software OpenPTV (Open PTV Software Consortium). It is used to perform the following set of operations: (1) Calibration of the multi-camera system (using the custom-fabricated 3D V-shaped target shown in Fig. 3). An expanded uncertainty in position of ± 1.5 mm in all directions is obtained, corresponding to a positional uncertainty ranging from ± 0.89 to ± 2.69 pixels throughout the system control volume; (2) Detection of the particle images: Firebrands 2D image coordinates are found using a pixel intensity-weighted centroid operator (confirmed to efficiently process glowing/hot particles); (3) Definition of particle correspondences across multi-camera views using the epipolar line intersection technique; (4) Computation of 3D particle coordinates in the object space; and (5) Particle tracking via spatio-temporal particle matching using both image and object space information. Further details about these steps can be found in the work of Maas (1991), Maas et al. (1993) and Willneff (2003).

Special attention was given to firebrand tracking efficiency and the recombination of broken trajectories. Although seldom, a broken trajectory can occur if a firebrand visibility becomes challenging (e.g., low glow versus very bright object in the background). Dedicated algorithms were developed to predict, within a user-specified temporal window, the missing positions of firebrands with early ended trajectories and identify sister trajectories by performing spatio-temporal matching in each particle image plane. Further details are provided in Bouvet et al. (2020) and the efficiency of such a trajectory recombination strategy is illustrated in Sect. 4.

In this work, Particle Image Densities (PIDs) on the order of 4×10^{-5} particles-per-pixel (ppp) are considered, which is similar to density estimates drawn up from available field work data [e.g., Filkov and Prohanov (2018)]. Such densities
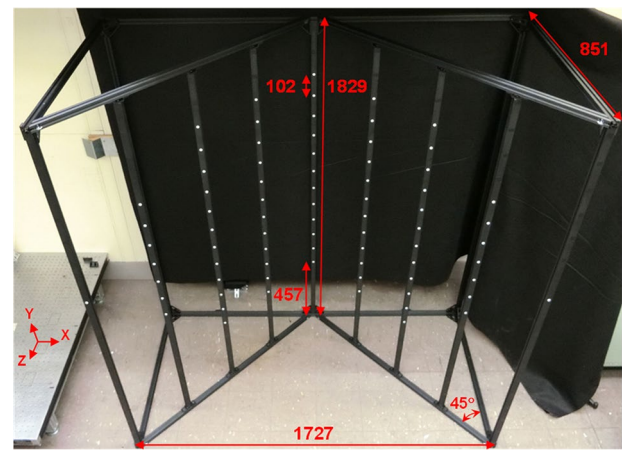
Fig. 3 3D spatial calibration target (dimensions in mm). The target contains 76 white dots with known 3D coordinates, all being visible from the system four viewpoints

are one to two orders of magnitude lower than those reported for large scale PTV experiments with controlled seeding (see, for instance, Rosi et al. (2014) with 2×10^{-4} ppp, and Biwole et al. (2009) with $\approx 1 \times 10^{-3}$ ppp), two orders of magnitude less than PIDs known to promote triangulation errors [$\approx 5 \times 10^{-3}$ ppp, see Maas et al. (1993)] and four orders of magnitude less than high PIDs requiring state-of-the-art Lagrangian tracking procedures (Schanz et al. 2016).

2.3 Firebrand sizing via 3D particle shape reconstruction (3D-PSR)

The sizing of airborne firebrands presents a challenge due to the variation of particle projected shapes (a.k.a. "silhouettes") depending on the viewpoint considered. Simply extracting averaged size/surface area information based on the different 2D views does not produce satisfactory results in terms of describing the true size and shape of complex particles. This limitation is inflated as a particle moves through the control volume since it may tumble and change its orientation with respect to the camera planes, therefore introducing a time dependence in the silhouette characterization. In the present work, a more robust sizing approach compared to 2D silhouette characterization was implemented: Each particle is reconstructed in 3D using combined views of the multi-camera system, following the principles of the *Visual Hull* concept (Laurentini 1994).

The 3D shape reconstruction and sizing of a particle include the following steps:

(1) Edge detection; the set of particle 2D image coordinates is retrieved from the 3D-PTV output and is used to locate the particle across the four views and perform a two-step particle boundary detection (using the
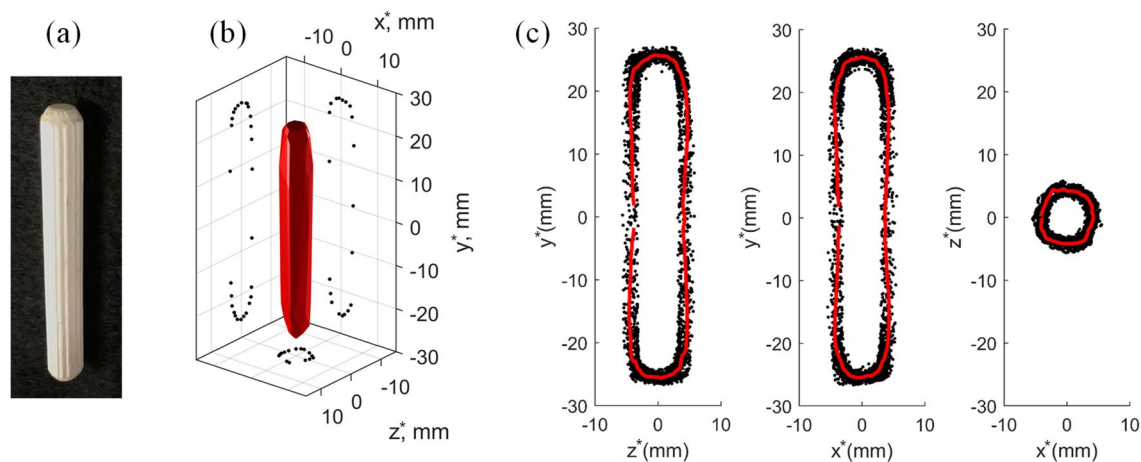
Fig. 4 Illustration of: **a** test particle; **b** extraction of outlines from a 3D test particle model (single timestep); **c** cumulative particle outline plots (all timesteps included). The red line indicates the average particle contour

corresponding silhouettes) as follows: i/ each image is first cropped and the median image from the prior 10 images is subtracted to improve particle isolation and remove background objects, ii/ particle boundary detection is performed using an unsupervised threshold selection for image segmentation (Otsu 1979).

(2) 3D shape reconstruction; particle boundaries obtained from the previous step are translated to the known 3D location of the particle in the object space[2] and rescaled according to the resolution calibration function to yield their true size. This calibration function, obtained via a dedicated procedure specified in Bouvet et al. (2020), leads to an uncertainty of at most 0.1 mm/pixel for locations situated the farthest away (≈ 2.4 m) from the camera image planes. Projection cones, whose apexes are defined by the camera perspective centers and profiles set by convex envelopes formed around the particle boundaries[3] in the object space, are created. The volume defined by the intersection of the four cones represents the 3D shape of the particle. A 3D model of the particle can be reconstructed using a dedicated Monte Carlo approach. This approach consists in randomly generating points within a localized search box containing the volume of intersection and retaining only those belonging to the latter. The resulting cloud of data points defines the particle convex hull, and the

shell formed by the outermost points can be saved and used for sizing purposes. For the present application, a sampling point density of 40 points/mm³ was chosen as optimal value in order to balance computational time and volume reconstruction accuracy ($> 95\%$ of the true hull volume).

(3) Aggregation of 3D reconstruction; because of the stochastic nature of the image backgrounds and the orientations of airborne firebrands, it is highly desirable to use all available 3D reconstructions (typically ≈ 10 models). Principal component analysis is used to identify the main axis of all generated point clouds and re-orient them accordingly. Scatter plots of the particle contours can be created by performing orthogonal projections of the data points located on the outer boundaries of each individual hull, for each orthogonal view considered. The outline projection of a test particle (white stick, shown in Fig. 4a) is illustrated in Fig. 4b for a single timestep reconstruction. Figure 4c shows cumulative plots with all available outlines from which sizing characteristics can be extracted.

It is important to stress that the accuracy of the particle sizing (step 3) is closely related to that of both the image thresholding (step 1) and the Visual Hull reconstruction (step 2) techniques. The Otsu thresholding method was visually confirmed to perform very well overall in the current configurations. However, instances where a portion of the particle perfectly blends with the background may negatively influence edge detection in individual images. Additionally, individual particle orientations may hide critical features from the view of the fixed-position cameras, potentially introducing reconstruction inaccuracies. Aggregation of multiple observations of the same particle helps minimize

---

[2] The 2D centroid positions relative to the particle boundaries are preserved and matched with the 3D particle location. All coordinates are results of the 3D-PTV output.

[3] These convex envelopes can be visualized as the shapes that rubber bands would take if wrapped around the particle boundaries. This simplification greatly improves the problem computational tractability.

the weight of those sporadic cases in the final results. While a sizing accuracy cannot be stated solely based on the knowledge of the experimental layout (the accuracy will depend on factors unknown a priori such as the particle shape, flight-path, etc.), computational strategies to gain insight into detailed measurement accuracy could be explored (see discussion in Sect. 5).

3 Application to model firebrands in laboratory settings: validation cases

The system described above has been tested in a series of validation experiments using combusting (model embers) and non-combusting (white particles) objects. The following sub-sections give an overview of typical tests performed to assess proper implementation of the 3D tracking and sizing techniques. These tests, while relatively simple, are essential since the use of large-scale 3D-PTV systems using consumer-grade electronics presents many challenges as compared to scientific-grade systems commonly used in small-scale laboratory settings [e.g., camera temporal synchronization, see discussion in Lobutova et al. (2010)]. Additional details regarding the experimental setups and data processing parameters can be found in the supplementary information (see Online Resource 1).

3.1 Rotating firebrand stick

Proper 3D tracking was verified by monitoring the motion of a rotating punk stick, whose glowing lit end served as a model firebrand. The punk stick (≈ 3.6 mm thick) was attached to a metallic arm (≈ 397 mm length), itself mounted on the shaft of a gear box motor controlled by a DC power supply. The centerline of the motor shaft was set to coincide with the origin of the global coordinate system in the *XZ* plane. After lighting the end of the stick, the angular velocity was increased, and several rotations were observed until steady glowing was obtained. Data were then acquired, and the measurements were compared to the predicted trajectory of the model firebrand (inferred from the known dimensions in the experimental layout, defining the center of the model firebrand at mid height of the glowing spot). Overall, the agreement was found to be very good, with a measured radius and height of 396.2 mm $\pm$ 2.3 mm and 1526.9 mm $\pm$ 3.7 mm compared to the predicted values of 396.9 mm $\pm$ 5 mm and 1523.3 mm $\pm$ 5 mm, respectively. The agreement between the velocity measurement average (44.3 cm s^{-1} $\pm$ 1.9 cm s^{-1}) and its predicted value (44.3 cm s^{-1}) was found to be excellent given some imperfections in the validation setup (non-perfect load/motor inertia match, system not perfectly rigid, etc.) and the intended application.

3.2 Vertical release of spherical particles

A total number of 110 quasi-spherical particles were randomly released in space and time from a platform (50.8 cm $\times$ 76.2 cm) fitted with 19 equally distributed 16 mm diameter holes. The platform was located ≈ 1.65 m above the optical table and illumination was provided using a set of four 3200 lm LED lights judiciously located to ensure optimal lighting of the volume monitored. The particle set included the following size classes (the particle count and true diameter are provided between parenthesis): 6 mm (38, 6.2 mm $\pm$ 0.2 mm), 8 mm (36, 7.9 mm $\pm$ 0.3 mm), 10 mm (13, 9.9 mm $\pm$ 0.2 mm), 12 mm (10, 11.9 mm $\pm$ 0.2 mm), and 14 mm (13, 13.8 mm $\pm$ 0.4 mm). These classes essentially belong to the lower end of the particle size spectrum that can be investigated by the system described in Sect. 2. The size classes were specifically chosen in close proximity to provide stringent testing conditions and demonstrate the system ability to achieve fine size classification. Falling spheres were tracked and sized according to the methodologies detailed in Sect. 2.

Size distribution histograms are shown in Fig. 5a. Datasets for both measured ("Airborne" in blue) and known ("Sphere diam." in red) sizes are compared (overlap shown in purple). Measurements taken along the z^* and x^* axes agreed relatively well with the known sphere diameters. Note that a perfect match between the two datasets is not to be expected given that the chosen class width (2 mm) is on the order of the smallest resolution achieved (i.e., $\approx$ 1.6 mm/pixel in the back of the control volume) and that the unit area for particle silhouette detection is 1 pixel. In the present case, it was noticed that, depending on the view considered, nonuniform sphere surface area illumination could slightly bias the edge detection toward the inner silhouette boundaries (i.e., -1 pixel as compared to visual observations), which in turn explains the observed shifts toward the smaller size classes. On the other hand, some of the measurements taken along the y^*-axis fall in size classes that are well beyond the maximum sphere diameter. These overestimations are the result of a nonsystematic artifact of the Visual Hull reconstruction: given a particle property (shape, size, orientation and location within the control volume) and system layout (finite number of cameras, cameras location in space), blind volumes, not carved by the silhouette projection cones, might remain and contribute to the artificial enlargement of the particle. This is illustrated in Fig. 5b where a 3D reconstruction "worst case scenario" is presented for a 14-mm sphere bringing a contribution to the 20 mm class count of the *Airborne y** dataset. Added volumes in the front (*low y**) and back (*high y**) of the visual hull are clearly seen by comparing both known (blue) and reconstructed (red) sphere shapes. Similar observations were reported by Kleinkort et al. (2017) for a three- and a

(a)   **(b)**
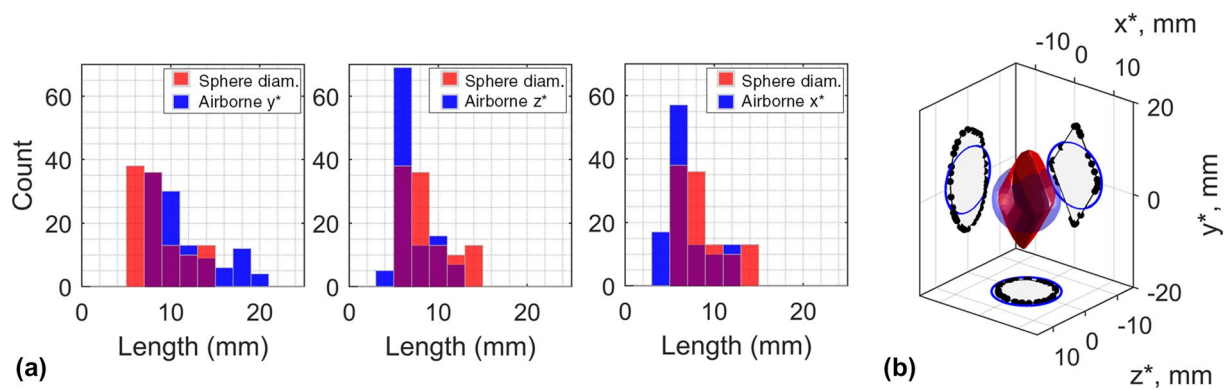
Fig. 5 Size distribution comparison: **a** known sphere sizes (*Sphere diam.*) versus measurements (*Airborne*) along the particle y^*, z^* and x^* axes, respectively (all axes mentioned are local to the re-oriented particle, size distribution overlaps are shown in purple); **b** Example of a 3D reconstructed sphere shape and its projected boundaries (in red, single time step) contributing to the 20-mm size class observed in the "*Airborne y^**" histogram. Actual sphere shape and its projected boundaries are shown in blue

five-camera system. Strategies to improve the current sizing approach, especially improving the Visual Hull reconstruction fidelity, are further discussed in Sect. 5.

4 Application to an artificially generated firebrand shower

4.1 Experimental layout and procedure

The emberometer was tested at the NIST National Fire Research Laboratory (NFRL). The experimental layout and procedure, similar to those described by Bouvet et al. (2018), are briefly described below. The emberometer was set downstream of a firebrand generator, following the arrangement shown in Fig. 6a. The generator, designed according to some of the specifications given by Manzello et al. (2008), is operated to produce firebrand "showers" whose particle number densities are visually consistent with field observations. Additional details regarding the firebrand generator used in this study are provided in Fig. 6b. In the present case, the fuel was 350 g ± 1 g of dry (moisture content < 6%) Douglas fir cuboids (side lengths: 7.8 mm, 8.1 mm, and 12.9 mm, ± 0.4 mm).

Firebrands were generated over a period of about 74 s. The analysis presented in the next section concentrates on a 35 s time window when the peak production of firebrands occurred. Most landing firebrands were collected in aluminum pans filled with water covering an area of about 2.4 m² starting 0.56 m downstream of the firebrand generator exit plane. Collected firebrands (999 count) were dried and their sizes measured to provide an independent dataset for firebrand size distribution comparison (if interested, the reader will find sample images for both airborne-tracked and ground-collected firebrands in the supplementary

information, see Online Resource 1). To support the airborne firebrand sizing analysis (and avoid counting broken tracks as independent particles), the trajectory recombination strategy described in Sect. 2.2 was applied. On a total number of 640 expected (complete) trajectories, 6.4% were found incomplete and were successfully recombined, and 0.8% could not be recombined.

4.2 Results

4.2.1 Firebrand 3D tracking and firebrand flux metric development

Figure 7 shows a cumulated plot of the 691 raw 3D trajectories reconstructed in the present case. A video displaying the time-resolved 3D motion of all firebrands is also provided in the supplementary information for enhanced legibility (see Online Resource 2). The system allows for the characterization of a wide range of firebrand dynamics, including low-velocity motion (< 0.4 m s^{-1}) of small embers (air draft/lift force sensitive) as well as projectile-like motion (> 4 m s^{-1}) of gravity-driven embers. The firebrand exposure can be quantified by monitoring the number of particles crossing a reference surface of defined geometry and location within the experimental control volume, therefore yielding a Cumulative Particle Count (CPC, unit: particles m^{-2}). In the present case, the reference surface is a disk, whose center is located at $X = -150$ mm, $Y = 1000$ mm, and $Z = 0$ mm and with a radius r equal to 200 mm (see Fig. 7). Both location and size were carefully chosen so that the reference surface was completely embedded within the core of the firebrand flow (i.e., in the region of high density of firebrand trajectories) at mid-height of the system control volume. Figure 8 shows the CPC versus time given the reference surface. The total CPC over the test period was close
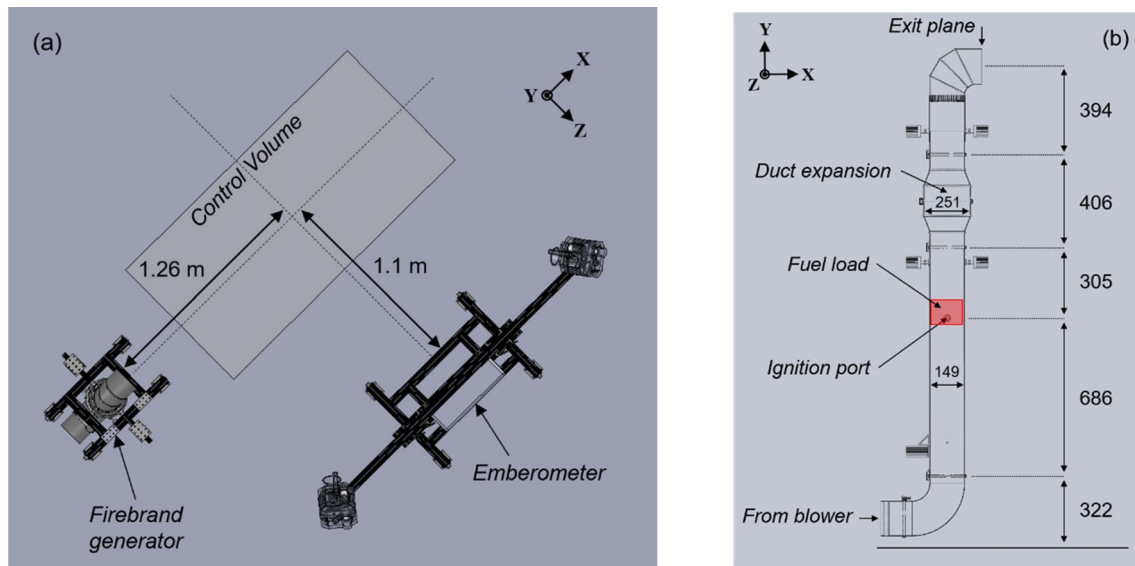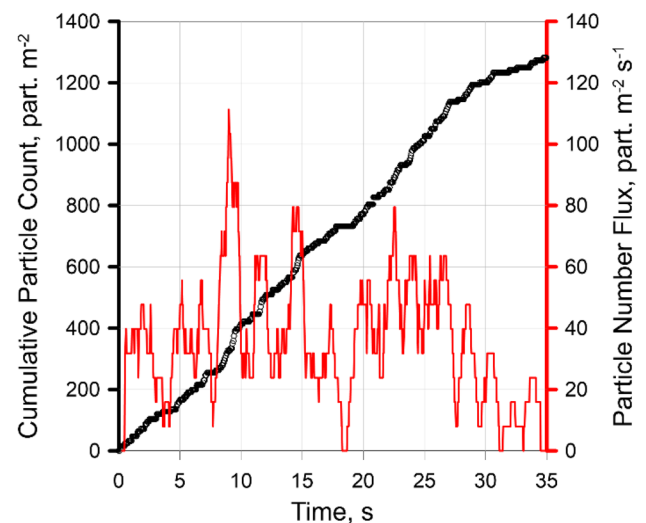
Fig. 6 Experimental layout for NFRL tests: **a** Top view; **b** Structure details of the firebrand generator (all dimensions in mm)
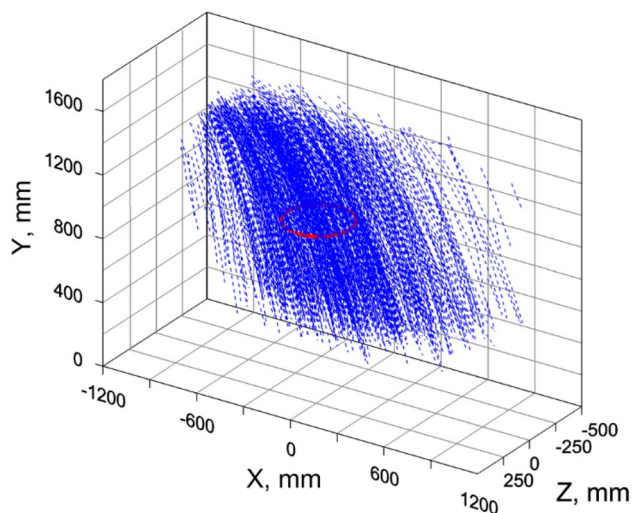
Fig. 7 Cumulated plot of firebrand 3D trajectories (trajectories are plotted with dotted lines to enhance legibility. The red circle defines the perimeter of the reference surface chosen for the particle number flux analysis, see Fig. 8. Center of the reference surface is located at $X = -150$ mm, $Y = 1000$ mm, and $Z = 0$ mm and its radius is equal to 200 mm)

Fig. 8 Cumulative Particle Count and corresponding Particle Number Flux versus time (derivations performed on a 30 timestep window, ≈ 1 s). The reference surface outline is shown in Fig. 7

to 1281 particles m^{-2}. This result is mildly affected by the choice of the disk surface, with a 15% increase/decrease in its surface area leading respectively to a 3.9% decrease / 5.2% increase of the CPC. The time-resolved CPC data can be used to derive the corresponding Particle Number Flux (PNF, unit: particles m^{-2} s^{-1}), which represents a number of particles per unit surface area, per unit time. It can be seen in Fig. 8 that the PNF peaked up to 111 particles m^{-2} s^{-1} at

$t = 9$ s, with most values falling within the 25–65 particles m^{-2} s^{-1} range throughout the test.

It is important to recognize that both CPC and PNF distributions, such as reported in Fig. 8, depend on the reference surface orientation and that the firebrand exposure perceived in the core flow cannot be fully characterized on the basis of a single surface orientation. As an example, a fictitious case, for which the firebrand flow is identical to the one described above, but with additional firebrands with trajectories parallel to the reference surface shown in Fig. 7, would yield identical CPC and PNF distributions, despite obviously
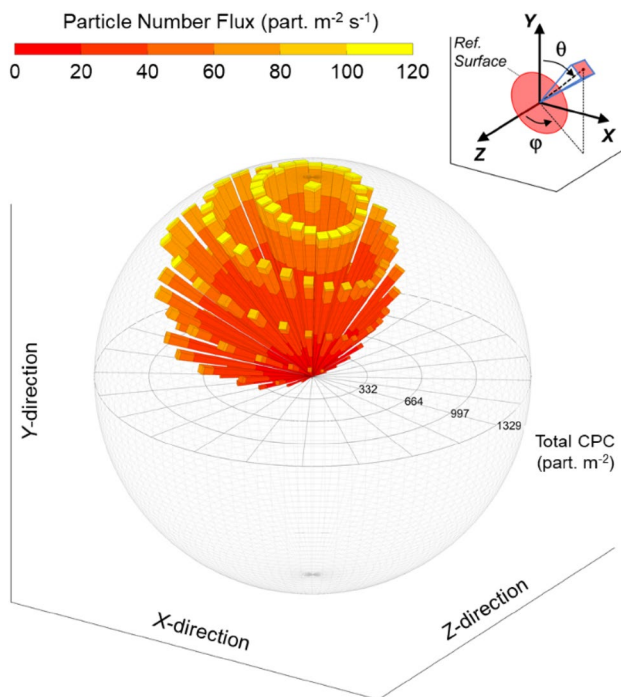
Fig. 9 3D "firebrand rose" graphic applied to the case presented in Sect. 4

different exposure levels. A complete characterization of the exposure therefore implies mapping both CPC and PNF distributions as functions of the reference surface orientation. To do so, the orientation of the reference surface is gradually changed by fixed angular increments (keeping the center of the surface constant—see additional details below) and the corresponding CPC/PNF datasets, such as shown in Fig. 8**,** are retrieved. These can be used to generate a 3D histogram (see Fig. 9), hereby referred to as "firebrand rose" (for its conceptual similarity with wind rose graphics), which delivers a synoptic view of the firebrand exposure over the entire test duration (in the present case, representative of the firebrand shower core). The properties of the bars that constitute the 3D firebrand rose are as follows:

(1) orientation: indicate the reference surface orientation set by both polar (θ) and azimuthal (φ) angles of the spherical coordinate system depicted in the insert of Fig. 9; the reference surface lays in a plane parallel to the bar's top surface. The center of the reference surface coincides with the origin of the spherical coordinate system. The angular increment is 15° in all directions;

(2) length: total CPC over the entire test duration. The circles in the sphere median plane indicate CPC iso-lines and the corresponding values are provided. The radius

of the outer spherical mesh matches the highest total CPC in any direction (i.e., 1329 particles m^{-2}).

(3) colored bins: each bar is divided into several bins whose colors correspond to the PNF ranges specified by the legend located to the right of the 3D histogram. The length of each bin is proportional to the cumulative time for which a PNF in the range indicated by the color was observed at the reference surface.

An animated view of the firebrand rose shown in Fig. 9 is provided to the reader in the supplementary information for enhanced legibility (See Online Resource 3). The firebrand rose displays an apparent symmetry about the *xy* plane of the spherical coordinate system which is consistent with the experimental configuration and the fact that the flow dynamics were unchanged during the entire duration of the test. The most severe exposure was obtained for orientations spanning ($\theta = 15°$, $\varphi = 225°$–$285°$) where total CPCs up to 1329 particles m^{-2} were recorded. For those cases, PNFs were higher than 40 particles m^{-2} s^{-1} for more than one third of the entire test duration. Taking the case ($\theta = 90°$, $\varphi = 270°$), which corresponds to a vertical surface parallel to the firebrand generator exit plane, the total CPC was found to drop down to ≈ 573 particles m^{-2}, with virtually no time period with PNFs higher than 40 particles m^{-2} s^{-1}. This comparison highlights the importance of scrutinizing the firebrand exposure problem in 3D and hence the usefulness of the firebrand rose representation. This is particularly relevant in practical situations whenever exposure severity assessment might be desired, for instance investigating building components with various orientations in space (e.g., gable vents, decking elements, roofing elements, etc.). In addition, the firebrand rose representation, because of its integrated format, is expected to facilitate comparisons between firebrand shower exposures arising from complex field situations that would be otherwise difficult to comprehend solely based on a 3D motion re-construction. These situations might include strong multidirectional motions of firebrands caused by abrupt wind changes, simultaneous lofting/deposition of small/large firebrands involving multiple generation spots, etc.

4.2.2 Artificial versus real wildland firebrand exposure: a comparison

The time-resolved characterization of firebrand flows rendered possible by the present system also sets an opportunity for assessing how realistic artificially generated firebrand fluxes are, with respect to prescribed or actual fire events. This is particularly relevant since there has been a growing interest in using firebrand generators in recent fire studies (Quarles and Standohar-Alfano 2018; Sharifian

and Hashempour 2016). However, it is generally unclear if the exposure levels generated match those encountered in wildland/WUI fires and, when considered, the question is solely addressed considering metrics that are uncorrelated with the firebrand flow dynamics and flux intensities [e.g., particle projected area vs. mass, see Manzello et al. (2008)]. While one must acknowledge that field data devoted to firebrand shower characterization is rather scarce, it is possible, under certain conditions, to perform meaningful firebrand flux comparisons between artificially generated and actual firebrand flows. An example is provided in the following by considering the present case and the recent investigation of Thomas et al. (2017), for which firebrand generation was studied during a prescribed fire ($\approx$ 7–13 MW m^{-1} intensity range) in a pine-dominated ecosystem. In the latter, durations for the period of peak firebrand collection were found to vary between 67 and 122 s depending on the collection site.[4] These durations can be used, instead of the more conventional "duration of collection" (i.e., the time elapsed between the arrivals of the first and last firebrands at monitored spots) to yield conservative[5] firebrand flux estimates that are not biased by periods of low firebrand activity. Doing so suggests that the highest firebrand flux experienced in the work of Thomas et al. (2017) was at most 7 particles m^{-2} s^{-1}. This exposure level can be compared to the present case provided that the corresponding PNF is extracted for matching conditions: (1) the reference surface orientation matches a ground collection configuration, i.e., ($\theta = 0°$, $\varphi = 0°$); (2) the height at which the reference surface is located matches a collection height of 120 mm [height of the collection cans in Thomas et al. (2017)]. In the present case, data are not directly available at this specific height, but the corresponding time-averaged PNF can be extrapolated using PNF datasets obtained at various heights in the core flow to account for the particle flow divergence. A PNF of 24.5 particles m^{-2} s^{-1} is found (21.5 particles m^{-2} s^{-1} taken into account the system Z-axis ground offset), which is more than 3 times the maximum exposure estimated for the work of Thomas et al. (2017). This result highlights the need for proper characterization of artificially generated firebrand flows whenever specific exposure conditions are to be replicated.

4.2.3 Firebrand 3D sizing

Figure 10 shows firebrand size distribution comparisons based on the emberometer measurements (*Airborne* firebrands, blue histograms) and the measurements taken on the firebrand population collected in the water pans (*Collected* firebrands, red histograms). In the latter case, given the 2D nature of the size analysis (justified by the fragility of the collected firebrands), only two dimensions, respectively labeled *Collected y** (longest dimension) and *Collected z** (smallest dimension), are used for the comparisons. Results pertaining to the combusting cuboids case detailed in the present section are displayed in the column (a). Results obtained for combusting sticks (pristine particle diam.: 6.6 mm $\pm$ 0.3 mm, length: 50.6 mm $\pm$ 0.1 mm) detailed in a preliminary study (Bouvet et al. 2018) are displayed in the column (b). The side by side comparison of the size distributions obtained for fuel batches with drastically different particle geometries builds confidence in the approach by identifying common areas of success and failure. It can be seen in Fig. 10 that the firebrand size distributions agree very well for two of the firebrand dimensions considered: the longest dimension, measured along the particle y^*-axis (1st row of Fig. 10) as well as one of the smaller dimensions (airborne x^*—see 3rd row of Fig. 10). This agreement is remarkable given the very narrow size class width selected (1 mm). Size distributions along the particle z^*-axis (2nd row of Fig. 10) suggest, however, that some of the emberometer measurements overestimate the actual firebrand size in this specific direction. This discrepancy, observed for both combusting cuboids and sticks, is the result of the nonsystematic artifact affecting the particle 3D reconstruction, as described earlier in Sect. 3.2. Note that in the present case, particle shrinkage due to combustion is not likely to be a factor that could explain the mismatch of the z^*-axis distributions, since the average flight time of a particle from the center of the control volume to the ground is on the order of 0.3 s. Particle breakage is also unlikely to play a significant role since size distribution in the other directions would have been equally affected.

5 Additional considerations

While the discussion provided in Sect. 4.2 essentially tackles the firebrand shower exposure in terms of number fluxes, the ability of the system to resolve individual particle volumes permits mass flux estimations provided that a particle average density is known. This knowledge could be inferred from previous experimental studies, e.g., Sánchez Tarifa et al. (1967), or indirectly, by considering scaling relations that might exist between a particle mass and its morphological attributes, as done by Tohidi et al.
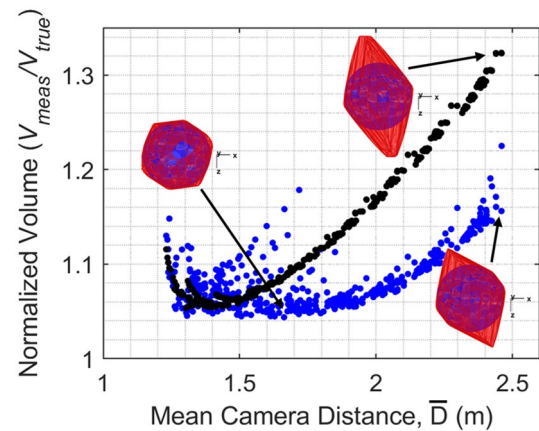
---

[4] All firebrand collection sites located outside of the controlled fire perimeter ($\approx$ 15 m away).

[5] The total number of firebrands collected for the entire duration of collection is used since no count of firebrand is provided for the firebrand shower peak events only.

(a)   **(b)**   Length (mm)
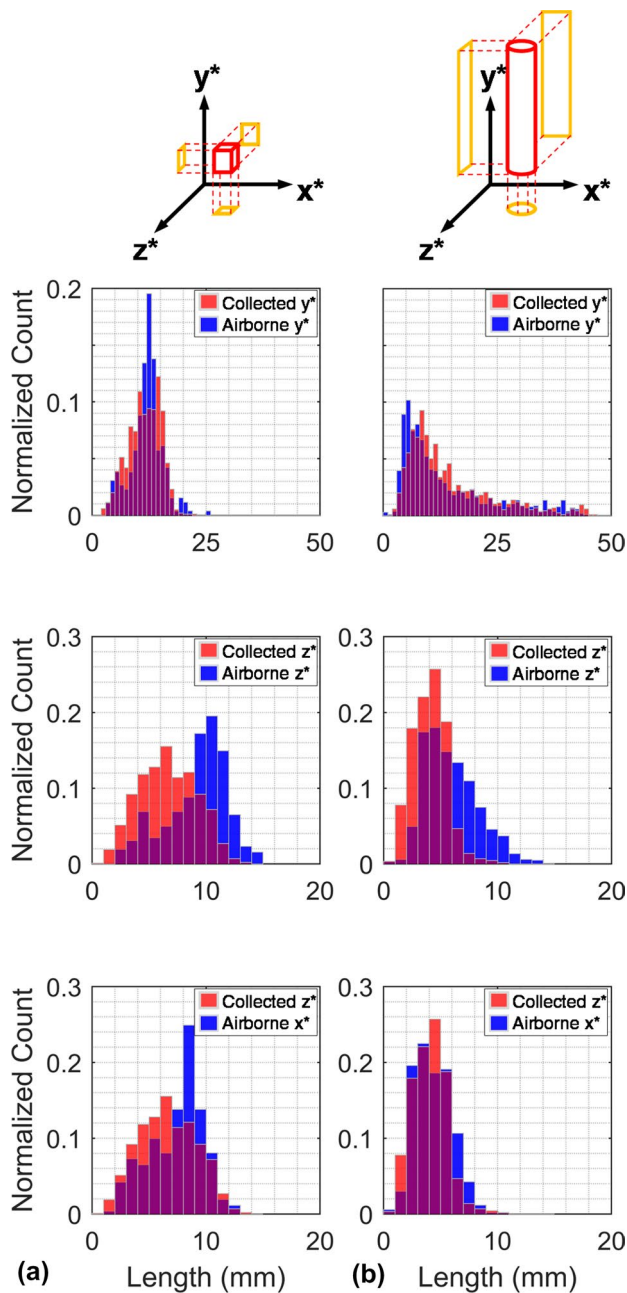
Fig. 10 Firebrand size distributions measured by the 3D-PTV/PSR system (airborne measurements, in blue) versus 2D ground collection analysis (water-quenched embers, in red), histogram overlap is shown in purple; case **a**: combusting cuboids (Sect. 4); case **b**: combusting sticks, results taken from the work of Bouvet et al. (2018) and re-plotted for ease of comparison. Schematics in the first line provides an example of particle orientations used for sizing operations

Fig. 11 Normalized volume (ratio of the reconstructed V_{meas} to the known V_{true} volumes) versus $\overline{D}$ (average of the distances from the camera perspective centers to the particle center) for a 25.4 mm fictitious sphere walked through the system control volume. Black dots: Camera #4 coordinates are (0.934 m, 0.312 m, 1.24 m)—original position; blue dots: Camera #4 coordinates are (0.934 m, 1.033 m, 0 m)—new position. Figure inlays show actual (blue) and reconstructed (red) volumes over imposed

(2015). In a real WUI fire context, the unknown nature of the firebrands (vegetative and/or structural matter) and their unknown thermal history (char vs. pristine fuel content) renders accurate mass flux estimates extremely challenging.

As previously alluded, the performance of the Visual Hull technique is related to a broad range of factors (particle- and system-specific). Among these, the camera 3D positions and orientation angles play an essential role. While the present camera layout has been selected to ensure system compactness (enhanced portability for deployment) and minimize measurement intrusiveness, it does not necessarily lead to the smallest hull reconstruction errors. Bringing one of the cameras away from the current acquisition plane can substantially improve the reconstruction process. This is illustrated in Fig. 11 where a fictitious spherical particle (25.4 mm diameter) was moved across the control volume and its visual hull systematically reconstructed. The operation was performed for two different positions of Camera #4, including its original position (0.934 m, 0.312 m, 1.24 m) and a new "out-of-plane" position (0.934 m, 1.033 m, 0 m) located to the right side of the system control volume. The normalized particle volume (ratio of the reconstructed to the actual volume) is plotted as a function of the effective distance $\overline{D}$, defined as the average of the distances from the camera perspective centers to the center of the particle. It can be seen in Fig. 11 that most of the datapoints for the new Camera #4 location are contained below the 15% volume overestimation level. This constitutes a marked improvement as compared to the results obtained for the original location (see inlays in Fig. 11 showing examples of reconstructed hulls). Future work will focus on optimizing camera placements to reach optimal hull reconstruction accuracy while maintaining system portability/non-intrusiveness. Some of the criteria proposed by Forbes (2007) will be further

investigated. In addition to camera placement in space, ways to further improve the system spatial calibration accuracy will be sought after. A volume self-calibration approach, such as the one detailed by Wieneke (2008), may be very efficient at improving both particle tracking and sizing accuracies. Adopting such an approach will require developing a dedicated calibration procedure to ensure that proper statistical analyses can be performed since typical particle densities in this work are several orders of magnitude lower than those required for successful self-calibration.

For a chosen camera configuration (finite number of cameras, known camera locations and known optical arrangement), the accuracy of the Visual Hull approach only depends on the particle specifics, i.e., the shape and size of the particle, its position within the monitored volume and its orientation. Except for the 3D position, these characteristics are unknown a priori for a random particle in motion, hence the extent to which the visual hulls are affected by reconstruction artifacts, as described in Sect. 3.2, is also unknown. Better understanding reconstruction errors introduced at each time step is essential to correct/remove any bias affecting the particle outline plots and, in turn, increase particle sizing robustness. To do so, a hybrid approach, that would rely both on particle Visual Hull reconstruction and particle shape classification using deep learning tools [cf. Rajagopalan et al. (2017)] seems very promising. Both particle shape and orientation could be determined by a properly trained classifier algorithm, paving the way for sizing bias correction, supported by synthetic data generation (as shown in Fig. 11).

6 Conclusion

A new three-dimensional (3D) measurement diagnostic tool, devoted to the characterization of airborne firebrands in the context of wildland and Wildland-Urban Interface (WUI) fires, has been developed. This tool, referred to as "emberometer", merges the following two imaging techniques: 3D Particle Tracking Velocimetry (3D-PTV), allowing for the time-resolved mapping of firebrand trajectories, and 3D Particle Shape Reconstruction (3D-PSR), used to build 3D models of individual firebrands based on the Visual Hull concept. This emberometer, designed as a self-contained/field-deployable system, offers the possibility to study time-resolved firebrand fluxes and firebrand size distributions to the full extent of their three-dimensional nature, for the first time removing the limitations of the ground collection approach.

The methodologies used in the present work were first validated in laboratory scale experiments, two of which have been reported herein: (1) a particle tracking validation, involving a setup with a lit punk stick with known trajectory and speed, and (2) a particle sizing validation, performed on a series of randomly released spheres (gravity-driven motion) with known diameters. In both cases, measurements were found to closely agree with the benchmark values, with the exception of the sphere size distribution along the particle $y*$-axis for the sizing validation (measurement overestimation). The observed discrepancy was traced back to the presence of extra volumes along the $y*$ axes of the particle hulls, a reconstruction artifact due to the current camera layout.

The emberometer was applied to an artificially generated firebrand shower, where the motions of nearly 700 firebrands were successfully reconstructed in 3D over a narrow time frame (35 s). The system was able to resolve a wide range of firebrand dynamics, with particle velocities ranging from tens of cm s^{-1} to several m s^{-1}. A novel 3D graphic representation that provides a synthetic view of the firebrand exposure magnitude was introduced. This representation incorporates both the Cumulative Particle Count (CPC, particles m^{-2}) and Particle Number Flux (PNF, particles m^{-2} s^{-1}) as orientation-dependent metrics, and hence is expected to facilitate exposure comparisons across different experiments. Its usefulness was illustrated by comparing the exposure level achieved in the present case to that of an experimental outdoor fire. Firebrand size distributions were also investigated and compared to a case previously discussed. Results showed that excellent agreement between the airborne (emberometer) and ground collection measurement approaches is generally achieved for two of the three firebrand characteristic dimensions. However, size distributions for the third dimension were found to be skewed toward larger sizes, a discrepancy attributed to the Visual Hull reconstruction artifact previously mentioned. Strategies to minimize this artifact, by modifying the current camera layout and performing systematic firebrand shape classification, were proposed.

References

Bermudez E, Panzar J, Oreskes B, Smith D, Shyong F (2017) A Santa Rosa woman died in the fires, her neighbors survived. Here are their stories. Los Angeles Times. https://www.latimes.com/projects/la-me-santa-rosa-hemlock/

Biwole PH, Yan W, Zhang Y, Roux J-J (2009) A complete 3D particle tracking algorithm and its applications to the indoor airflow study. Meas Sci Technol 20(11):115403. https://doi.org/10.1088/0957-0233/20/11/115403

Bouvet N, Link ED, Fink SA, Kuligowski ED (2018) On the use of time-resolved three-dimensional diagnostics to characterize fire-brand showers in the WUI. In: Viegas DX (ed) Advances in forest fire research 2018. Imprensa da Universidade de Coimbra, Coimbra, pp 826–836. https://doi.org/10.14195/978-989-26-16-506_91

Bouvet N, Link ED, Fink SA (2020) Development of a new approach to characterize firebrand showers during Wildland-Urban Interface (WUI) fires: a step towards high-fidelity measurements in three dimensions. NIST Technical Note 2093, National Institute of Standards and Technology, Gaithersburg, MD. https://doi.org/10.6028/NIST.TN.2093

Calfire (2020) Top 20 most destructive California wildfires. https://www.fire.ca.gov/media/11417/top20_destruction.pdf

El Houssami M, Mueller E, Filkov A et al (2016) Experimental procedures characterising firebrand generation in wildland fires. Fire Technol 52(3):731–751. https://doi.org/10.1007/s10694-015-0492-z

Filkov A, Prohanov S (2018) Particle tracking and detection software for firebrands characterization in wildland fires. Fire Technol 55(3):817–836. https://doi.org/10.1007/s10694-018-0805-0

Filkov A, Prohanov S, Mueller E et al (2017) Investigation of firebrand production during prescribed fires conducted in a pine forest. Proc Combust Inst 36(2):3263–3270. https://doi.org/10.1016/j.proci.2016.06.125

Forbes K (2007) Calibration, recognition, and shape from silhouettes of stones. Ph.D. thesis, University of Cape Town, Cape Town. https://www.dip.ee.uct.ac.za/publications/theses/PhDKeith.pdf

Insurance Institute for Business & Home Safety (2019) Embers cause up to 90% of home & business ignitions during wildfire events. https://ibhs.org/ibhs-news-releases/embers-cause-up-to-90-of-home-business-ignitions-during-wildfire-events/

Jolly WM, Cochrane MA, Freeborn PH et al (2015) Climate-induced variations in global wildfire danger from 1979 to 2013. Nat Commun 6:7537. https://doi.org/10.1038/ncomms8537

Kleinkort C, Huang G-J, Bringi VN, Notaroš BM (2017) Visual Hull method for realistic 3D particle shape reconstruction based on high-resolution photographs of snowflakes in free fall from multiple views. J Atmos Ocean Technol 34(3):679–702. https://doi.org/10.1175/jtech-d-16-0099.1

Laurentini A (1994) Visual hull concept for silhouette-based image understanding. IEEE Trans Pattern Anal Mach Intell 16(2):150–162. https://doi.org/10.1109/34.273735

Lobutova E, Resagk C, Putze T (2010) Investigation of large-scale circulations in room air flows using three-dimensional particle tracking velocimetry. Build Environ 45(7):1653–1662. https://doi.org/10.1016/j.buildenv.2010.01.016

Luhmann T, Robson S, Kyle S, Boehm J (2014) Close range photogrammetry and 3D imaging. Walter De Gruyter GmbH, Berlin/Boston

Maas HG (1991) Digital photogrammetry for determination of tracer particle coordinates in turbulent flow research. Photogramm Eng Rem Sens 57(12):1593–1597

Maas HG, Gruen A, Papantoniou D (1993) Particle tracking velocimetry in three-dimensional flows. Exp Fluids 15(2):133–146. https://doi.org/10.1007/bf00190953

Manzello SL, Maranghides A, Mell WE (2007) Firebrand generation from burning vegetation. Int J Wildland Fire 16(4):458–462. https://doi.org/10.1071/WF06079

Manzello SL, Shields JR, Cleary TG et al (2008) On the development and characterization of a firebrand generator. Fire Saf J 43(4):258–268. https://doi.org/10.1016/j.firesaf.2007.10.001

Manzello SL, Maranghides A, Shields JR, Mell WE, Hayashi Y, Nii D (2009) Mass and size distribution of firebrands generated from burning Korean pine (*Pinus koraiensis*) trees. Fire Mater 33(1):21–31. https://doi.org/10.1002/fam.977

Open PTV Software Consortium, OpenPTV. http://www.openptv.net. https://doi.org/10.5281/zenodo.2646623

Otsu N (1979) A threshold selection method from gray-level histograms. IEEE Trans Syst Man Cybern 9(1):62–66. https://doi.org/10.1109/TSMC.1979.4310076

Quarles SL, Standohar-Alfano CD (2018) Wildfire Research—ignition potential of decks subjected to an ember exposure. Technical report, Insurance Institute for Business & Home Safety. https://ibhs.org/wp-content/uploads/Ignition-Potential-of-Decks-Subjected-to-an-Ember-Exposure.pdf

Rajagopalan AK, Schneeberger J, Salvatori F et al (2017) A comprehensive shape analysis pipeline for stereoscopic measurements of particulate populations in suspension. Powder Technol 321:479–493. https://doi.org/10.1016/j.powtec.2017.08.044

Rosi GA, Sherry M, Kinzel M, Rival DE (2014) Characterizing the lower log region of the atmospheric surface layer via large-scale particle tracking velocimetry. Exp Fluids 55(5):1–10. https://doi.org/10.1007/s00348-014-1736-2

Sánchez Tarifa C, Pérez Del Notario P, García Moreno F, Rodriguez Villa A (1967) Transport and combustion of firebrands—Volume II. Final Report of Grants FG-SP-114 and FG-SP-146 (Vol. II), Instituto Nacional de Tecnica Aeroespacial «Esteban Terradas», Madrid, Spain

Schanz D, Gesemann S, Schröder A (2016) Shake-The-Box: Lagrangian particle tracking at high particle image densities. Exp Fluids 57(5):70. https://doi.org/10.1007/s00348-016-2157-1

Sharifian A, Hashempour J (2016) A novel ember shower simulator for assessing performance of low porosity screens at high wind speeds against firebrand attacks. J Fire Sci 34(4):335–355. https://doi.org/10.1177/0734904116655175

Thomas JC, Mueller EV, Santamaria S et al (2017) Investigation of firebrand generation from an experimental fire: development of a reliable data collection methodology. Fire Saf J 91:864–871. https://doi.org/10.1016/j.firesaf.2017.04.002

Tohidi A, Kaye N, Bridges W (2015) Statistical description of firebrand size and shape distribution from coniferous trees for use in Metropolis Monte Carlo simulations of firebrand flight distance. Fire Saf J 77:21–35. https://doi.org/10.1016/j.firesaf.2015.07.008

Tohidi A, Gollner MJ, Alfano C, Quarles Q (2017) Computer vision techniques for firebrand detection and characterization. In:16th international conference on automatic fire detection and the suppression, detection and signaling research and applications (SUPDET 2017), Sept. 12–14, Hyattsville, MD

Vodvarka FJ (1970) Urban burns—full scale field studies. Final Technical Report—Project J6171, IIT Research Institute, Chicago, IL

Waterman TE (1969) Experimental study of firebrand generation. Final Technical Report—Project J6130, IIT Research Institute, Chicago, IL

Wieneke B (2008) Volume self-calibration for 3D particle image velocimetry. Exp Fluids 45:549–556. https://doi.org/10.1007/s00348-008-0521-5

Willneff J (2003) A spatio-temporal matching algorithm for 3D particle tracking velocimetry. Ph.D. thesis, Swiss Federal Institute of Technology Zurich, Zurich. https://ethz.ch/content/dam/ethz/special-interest/baug/igp/igp-dam/documents/PhD_Theses/82.pdf

Authors and Affiliations

Nicolas Bouvet[1] · **Eric D. Link[1]** · **Stephen A. Fink[1]**

✉ Nicolas Bouvet
   nicolas.bouvet@nist.gov

[1] National Institute of Standards and Technology (NIST), 100 Bureau Drive, Gaithersburg, MD 20899, USA